JACS
JOURNAL OF THE AMERICAN CHEMICAL SOCIETY
pubs.acs.org/JACS
Article

Crystallographic Dimensionality Determines the Electrochemical Reaction Mechanism in Alkali Transition-Metal Chlorides

Michael A. Spencer, Tae Gyu Yun, Marguerite Flynn, Marie-Liesse Doublet, and Alexis Grimaud*

Cite This: J. Am. Chem. Soc. 2024, 146, 32059−32071
Read Online

ABSTRACT: Intense research efforts on transition metal chalcogenides (oxides and sulfides), pnictides (nitrides and phosphides), and fluorides have demonstrated the complex, intertwined effects of structural and chemical changes on their electrochemical response leading to intercalation, conversion, or displacement reactions when reacting with lithium. Prior efforts largely left halides unexplored due to their heightened solubility in classical liquid electrolytes. In this work, we employ superconcentrated electrolytes to demonstrate the composition- and structure-dependent electrochemical reactivity of A_2MCl_4 compounds (A = Li or Na and M = Cr, Mn, Fe, and Co). Comparing four lithiated compounds, we demonstrate that they all undergo conversion reactions when reacting with 2 Li^+ per formula unit, associated with large polarization and limited cycling ability. Nevertheless, combining in situ XRD with post-mortem XPS and STEM/EDS analysis, we demonstrate that Li_2CoCl_4 first reacts with one Li^+ following a displacement reaction providing a reversible capacity of 125 mAh g^{-1}. This reaction is enabled by the formation of a Li_6CoCl_8 intermediate, which shares a similar anionic framework with pristine Li_2CoCl_4, ensuring the topotactic insertion of Li^+ balanced by the Co^{2+}/Co^0 redox couple and the formation of metallic Co nanoparticles. Comparing these compounds, we propose that two criteria are necessary to trigger the displacement reaction in A_2MCl_4 compounds: the presence of 1D chains of edge-sharing octahedra to favor electronic delocalization and the availability of a metal-deficient intermediate. Screening numerous A_2MCl_4 compounds, we demonstrate the universality of these design principles, which extend to Na-ion materials by demonstrating a low-polarization, reversible displacement reaction for Na_2MnCl_4.

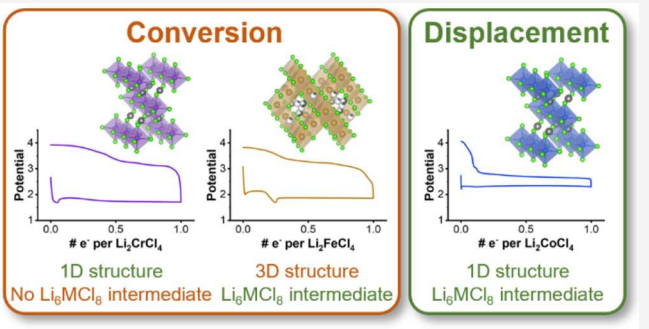

1. INTRODUCTION

Electrochemical insertion and conversion reactions enable a broad range of technologies, particularly electrochemical energy storage devices that power electric vehicles and portable electronics. The ionocovalent bonding character between the transition metal (TM) and anionic ligands underpins the redox activity of a material.[1] Chemical composition and crystal structure provide two knobs to control the ionocovalence of the TM-ligand bonds and are commonly used to tune the performance of cathode materials in lithium- and sodium-ion batteries. Following the pioneering works by Whittingham and Goodenough,[2−9] layered or spinel TM chalcogenides (oxides and sulfides) remain the stellar materials for the reversible (de)intercalation of Li^+. Nevertheless, reactivity of TM chalcogenides with lithium is not limited to (de)intercalation and different lithium uptake mechanisms such as displacement or conversion reactions were shown for binary TM oxides and sulfides.[10−14] Most other binary TM ligand materials, e.g., nitrides, phosphides, and fluorides, crystallize in fluorite, antifluorite, or hexagonal structures, among others, and undergo a conversion reaction upon reactivity with lithium.[15−19] However, careful studies over the course of multiple decades have revealed subtle deviations from conversion reaction for binary compounds such as FeF_3, which initially react with lithium following combined insertion and displacement reactions to form intermediates with composition $Li_xFe_{1-\delta}F_3$ along with FeF_2.[20] Moreover, subsequent conversion of FeF_2 was shown to proceed through a transient intermediate forming a $FeF_2|Li_2FeF_4|LiF$ interface that facilitates the nucleation and growth of LiF. Similarly, binary TM phosphides such as Ni_2P or FeP_y (y = 1, 2, or 4) were shown to react with lithium following a stepwise process involving the formation of a lithiated intermediate ($Li_{2.4}NiP_2$ and LiFeP, respectively).[21] Instead, ternary pnictides Li-TM-Pn systems (with TM = V, Ti, Fe, or Mn and Pn = N, P, or As) were shown to undergo reversible Li^+ (de)intercalation, associated with an amorphization/recrystallization of the structure upon cycling.[21−27] While not exhaustive, these few

Received: September 18, 2024
Revised: October 30, 2024
Accepted: October 31, 2024
Published: November 11, 2024

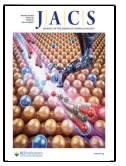

https://doi.org/10.1021/jacs.4c13005
J. Am. Chem. Soc. 2024, 146, 32059−32071

examples highlight the significant gap in knowledge that remains for the electrochemical reactivity of transition metal halides (e.g., chlorides, bromides, and iodides). This gap is largely explained by their solubility in traditional electrolytes, which has thus far limited such compounds to be used as cathodes in molten-salt batteries[28] or as solid electrolytes using redox inactive elements.[29]

Recently, it was demonstrated that a high concentration electrolyte, 5 M lithium bis(fluorosulfonyl)imide (LiFSI) in dimethyl carbonate (DMC), suppressed the solubility of vanadium trihalides (VX_3; X = Cl, Br, I) and enabled the reversible intercalation of up to 1 Li^+ per formula unit.[30] Further electrochemical studies coupled with structural characterization revealed that the layered VX_3 compounds with the O1 stacking structure undergo reversible lithium-ion insertion with anion-dependent structural transitions. This discovery significantly broadens the library of cathode chemistries available to be studied in liquid electrolytes and provides an avenue for deeper fundamental insights into how the characteristics of the anionic ligand (e.g., electronegativity, charge, ionic radius) influence electrochemical charge storage behavior (e.g., reaction mechanism, structural transitions, charge transport kinetics).

The discovery that transition metal halides can be stabilized in high concentration electrolytes opens up new chemistries with redox potentials between those found in oxides and sulfides owing to the intermediate electronegativities of Cl, Br, and I between that of O and S.[18,29,31] The chlorides offer the highest redox potentials compared to the bromides and iodides as well as greater theoretical gravimetric capacity. Transition-metal chlorides are reported to crystallize in a range of structural dimensionalities (defined by the connectivity of the transition metal chloride polyhedra) from 0D with isolated TM chloride polyhedra to 3D with TM chloride polyhedra interconnected in all directions throughout the lattice (Figure 1). Within the A_2MCl_4 stoichiometry, where A = alkali cation and M = metal cation, there are 0D, 1D, and 3D structures reported depending on the choice of A and M. Early studies on Li_2MCl_4 compounds focused on their ionic conduction properties, with conductivities measured on the order of 10^{-6} S cm^{-1} at room temperature and up to 10^{-2} S cm^{-1} at high temperatures after undergoing a transition from cubic inverse spinel to the cubic defect rocksalt-type structure.[31] Besides being studied as solid electrolytes, few reports have investigated Li_2MCl_4 compounds as electrode materials, all of them using solid-state electrolytes.[32−35] Tanibata et al. demonstrated that Li^+ can be deinserted from Li_2FeCl_4 with an initial charging capacity of 126 mAh g^{-1} and discharge capacity of 100 mAh g^{-1} at 30 °C using a $LiAlCl_4$ solid electrolyte.[34] Hao and Ma studied the influence of the composition of Zr in $Li_{2-2x}Mn_{1-x}Zr_xCl_4$ ($0 < x < 0.6$) on the ionic and electronic conductivity and electrochemical reactivity using the combination of Li_3InCl_6 and Li_6PS_5Cl solid electrolytes.[35] $LiMn_{0.5}Zr_{0.5}Cl_4$ showed the highest ionic conductivity, and electrochemical cycling revealed that Li^+ deinsertion is not possible. Further reduction led to a discharge capacity of 52.4 mAh g^{-1}, which quickly degraded during subsequent cycles. Although these studies show that electrochemical reactivity in A_2MCl_4 compounds is possible, little is known about the reaction mechanisms. Moreover, owing to the solubility of these phases in traditional/commercial liquid electrolytes, nothing is known regarding their electrochemical behavior in liquid electrolytes.

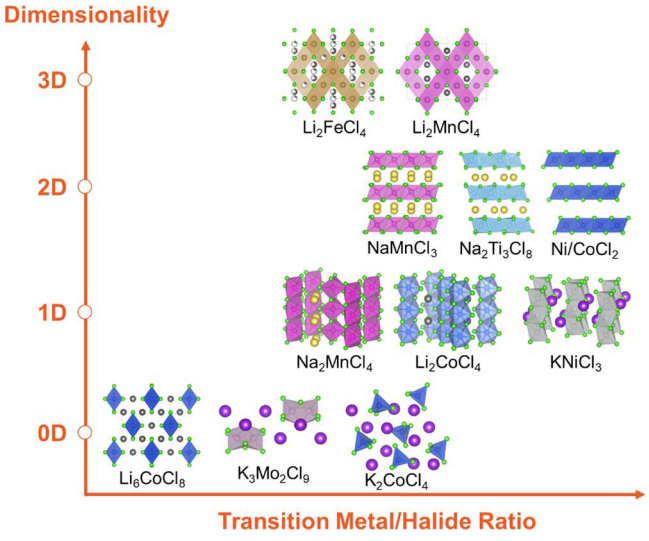

Figure 1. Collection of reported alkali transition-metal halides that contain crystallographic features ranging in dimensionality from 0D to 3D.

In this work, we utilized high concentration electrolytes that suppress the solubility of transition metal halide compounds to investigate the electrochemical reactivity of the A_2MCl_4 family of compounds. Electrochemical studies reveal limited or even negligible Li-ion deinsertion during oxidation for all A_2MCl_4 compositions. Strikingly, composition- and structure-dependent electrochemical behavior was observed upon reduction of the A_2MCl_4 phases, with some phases undergoing conversion with limited reversibility while others show reversible cycling with low polarization. Combining electrochemical measurements with in situ XRD, ex situ STEM/EDS, XPS experiments, and first-principles DFT calculations, we determined that the low polarization reactivity of some A_2MCl_4 halides is due to a displacement reaction and developed the guiding principles that unlock this reversible displacement reaction. Furthermore, we validated these criteria, which were based on Li-containing materials, by extending them to a Na-based compound that shows a reversible displacement reaction when cycled in superconcentrated Na-ion electrolyte. In summary, this work demonstrates the applicability of these structure−property relationships to design novel halide-based A_2MCl_4 materials in liquid electrolytes.

2. METHODS

Chemicals. LiCl (99%, Thermo Scientific) and NaCl (99.5%, Thermo Scientific) were dried at 55 °C under vacuum at 50 mbar for 24 h in a Buchi glass oven before transferring into an argon-filled glovebox for further processing. Binary transition metal chloride precursors were used as received, including $CrCl_2$ (97%, Thermo Scientific), $MnCl_2$ (99.99% metals basis, Thermo Scientific), $FeCl_2$ (99.5% metals basis, Thermo Scientific), $CoCl_2$ (97%, Sigma-Aldrich), and $CuCl_2$ (99.995% metals basis, Thermo Scientific).

Synthesis of A_2MCl_4 Phases. Li_2MCl_4 (M = Cr, Mn, Fe, Co), Li_6CoCl_8, and Na_2MnCl_4 were synthesized by mechanochemical synthesis using binary chloride (MCl_2) mixed with LiCl or NaCl. A typical mechanochemical synthesis involved the following steps: (1) grind precursors using a mortar and pestle; (2) load the mixture into a hardened stainless steel ball mill vial (SPEX 8009SS); (3) ball mill for 10 cycles with 30 min of milling and 30 min of resting per cycle (SPEX 8000 M mixer/miller); and (4) heat at 264 °C for 3 h on a hot

https://doi.org/10.1021/jacs.4c13005
J. Am. Chem. Soc. 2024, 146, 32059−32071

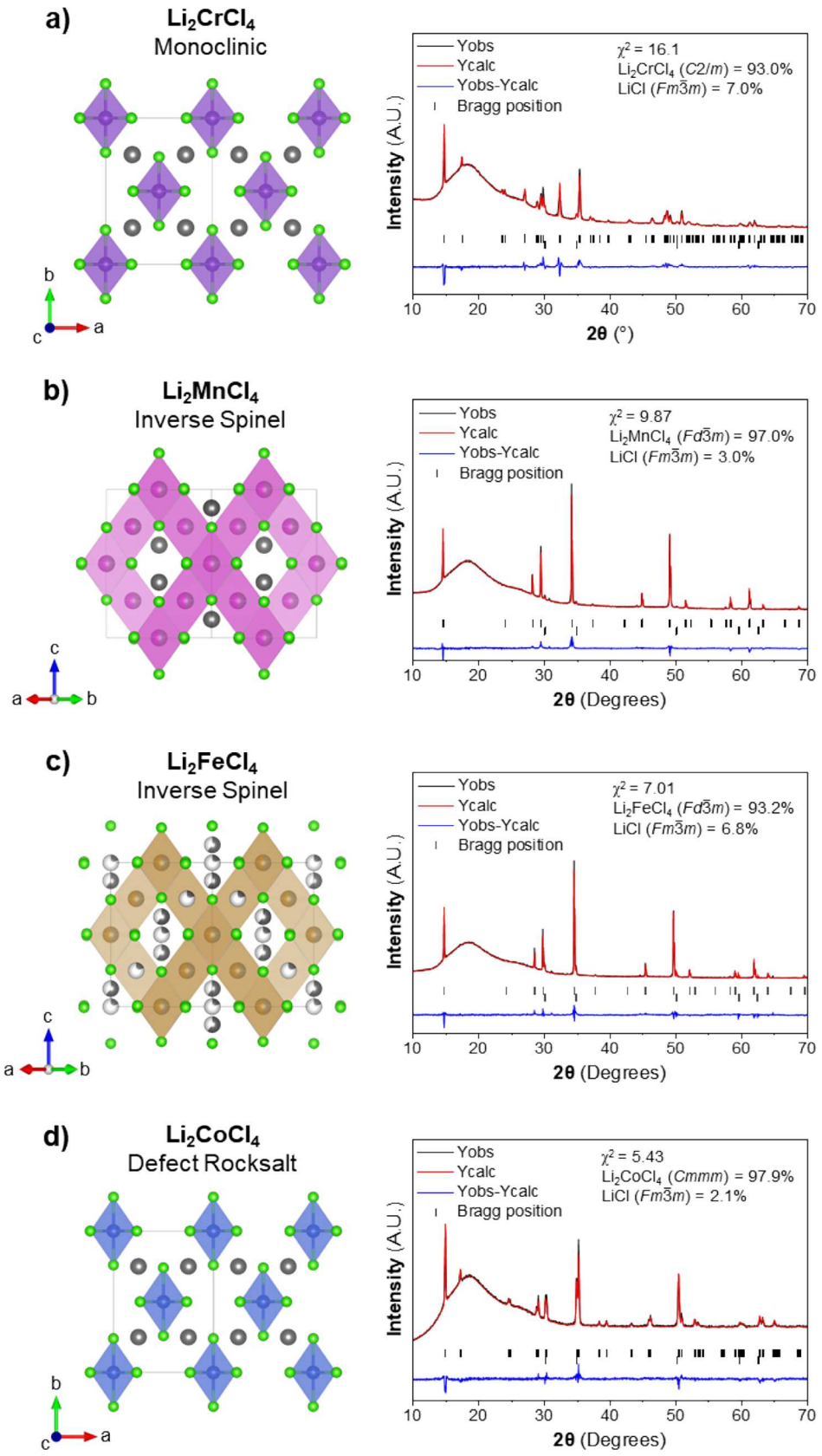

Figure 2. Crystal structures and XRD patterns with Le Bail fitting of (a) Li_2CrCl_4, (b) Li_2MnCl_4, (c) Li_2FeCl_4, and (d) Li_2CoCl_4. Black, red, and blue lines represent the observed, calculated, and difference patterns, respectively. Vertical tick marks indicate reflection positions.

plate.[33] Steps 1, 2, and 4 were performed in an argon-filled glovebox (MBraun, < 0.5 ppm of H_2O, O_2).

Physical Characterization. X-ray diffraction (XRD) measurements were performed using a Bruker D2 Phaser with Cu $K_{\alpha1}/K_{\alpha2}$

https://doi.org/10.1021/jacs.4c13005
J. Am. Chem. Soc. 2024, 146, 32059−32071

incident X-rays (λ_1 = 1.5406 Å, λ_2 = 1.5444 Å). Samples for XRD were prepared in an argon-filled glovebox in an airtight sample holder (MTI Corporation) with a Kapton window. In situ XRD measurements were carried out using a coin cell with a Kapton window (TCH Instrument). A background curve was manually generated and either fit or subtracted from each pattern to account for the large background from the Kapton window. The collected diffraction patterns were analyzed using the Le Bail fitting method in the FullProf Suite (version 5.10, 2023).[36] Each pattern was fit with the LiCl ($Fm\bar{3}m$) structure and the respective Li_2MCl_4 structures reported in the Inorganic Crystal Structure Database (ICSD). Crystal structure illustrations were produced using VESTA.[37]

X-ray photoelectron spectroscopy (XPS) measurements were conducted on a Thermo Fisher Scientific K-alpha instrument with an Al X-ray source. Pristine and ex situ powder samples were pressed into a copper holder and mounted in a vacuum transfer chamber in an argon-filled glovebox to avoid exposure to air and moisture. Data fitting and analysis was performed using Avantage software.

Transmission electron microscopy was performed on a Thermo Fisher Scientific Themis Z G3 Cs-corrected scanning transmission electron microscope equipped with a Super X-4 quadrant energy-dispersive X-ray spectroscopy (EDS) detector. Samples were prepared by sonicating in hexanes for ∼30 min and drop casting on a copper grid coated with lacey carbon (Oxford Instruments). Sample grids were loaded in the Mel-Build Atmos Double Tilt LN2 Vacuum/Inert Gas Transfer Holder in a nitrogen-filled glovebox and transferred to the TEM without any air/moisture exposure. High-angle annular dark field (HAADF) images and EDS mapping data were collected at 200 kV.

Electrochemical Characterization. Electrochemical measurements were performed using a Bio-Logic BCS-805 battery cycler. The active material was mixed with Super P carbon in a 7:3 weight ratio. Half cells were assembled using 2032 304 steel coin cells (TMAX) with aluminum foil coating the current collector at the positive electrode followed by the active material powder mixture, glass fiber separators (Whatman), 100 μL of 5 M LiFSI in DMC (Solvionic), polished lithium metal (MTI) on a stainless steel spacer, and a stainless steel spring. The coin cells were crimped with a pressure of 0.8 tons. Powder processing was carried out in an argon-filled MBraun Labstar Pro glovebox with <0.5 ppm O_2,H_2O. All coin cells were assembled in an argon-filled MBraun Unilab Pro glovebox with <0.1 ppm O_2/H_2O. Unless otherwise stated, galvanostatic cycling was conducted in a temperature control unit (Memmert) at a rate of C/10, with C referring to the exchange of 1 e^- per formula unit of the A_2MCl_4 compound. The C-rate was C/20 and rest time was 2 h during the galvanostatic intermittent titration technique (GITT) measurements.

Computational Details. Spin-polarized DFT calculations were performed using VASP.[38,39] The atoms are described in plane-wave basis sets using PAW pseudopotentials.[40] DFT(PBE)+U[41,42] with U_{eff}(Co) = 3 eV and metaGGA(SCAN)[43] functionals were checked and give very similar results. The inserted $Li_{2+x}CoCl_4$ and displaced $Li_{2+x}Co_{1-x/2}Cl_4$ phases were computed in large supercells (up to 225 atoms) with different Li distributions over the available sites. All atomic coordinates and lattice parameters were fully relaxed until the force acting on atoms is less than 5×10^{-3} eV Å^{-1}. The phase stability diagram comparing insertion, displacement, and conversion reaction energies was computed using the converted electrodes as the reference zero energy: $(1 - x/2)\ E(Li_2CoCl_4) + (x/2)\ E(Co° + 4LiCl)$ and only the most stable structures were considered.

3. RESULTS AND DISCUSSION

Alkali transition metal chlorides of the stoichiometry A_2MCl_4 (where A = alkali metal; M = transition metal) make up a compositionally and structurally diverse family of materials. Cations A and M occupy a combination of tetrahedral and octahedral positions in a closely packed anion sublattice. Owing to the nature of the metal-chloride bonds, a series of Li_2MCl_4 (M = Cr, Mn, Fe, Co) compounds, shown in Figure 2, were synthesized via ball milling and subsequent mild heating at 264 °C. Li_2CrCl_4 forms a monoclinic $C2/m$ structure with 1-dimensional (1D) chains of edge-sharing $CrCl_6$ octahedra parallel to the c-axis.[44] The $CrCl_6$ octahedral distortion leading to monoclinic symmetry is attributed to the Jahn−Teller effect. Li_2MnCl_4 and Li_2FeCl_4 both form cubic inverse spinel type ($Fd\bar{3}m$) structures.[45,46] In Li_2MnCl_4, half of the Li occupies the 8a tetrahedral position, while the other half shares the 16d octahedral position with Mn. In Li_2FeCl_4, the 16d position is half lithium and half Fe, while the remaining lithium occupies 8a tetrahedral and 16c octahedral positions. Li_2CoCl_4 forms the orthorhombic ($Cmmm$) defect rock-salt structure.[47] All Li and Co atoms occupy octahedral positions, with the $CoCl_6$ octahedra forming 1D edge-sharing chains parallel to the c-axis. These four materials consist of two inverse spinel structures with 3D interconnected MCl_6 octahedra (Li_2MnCl_4 and Li_2FeCl_4) and two structures with 1D chains of MCl_6 octahedra (Li_2CrCl_4 and Li_2CoCl_4), thus providing a set of materials suitable for studying the influence of dimensionality on the electrochemical reactivity of halide compounds with Li.

To investigate the electrochemical reactivity of the Li_2MCl_4 phases, a high concentration electrolyte (5 M LiFSI in DMC) previously shown to suppress the solubility of transition-metal halides was used.[30] We first investigated the $M^{2+/3+}$ redox

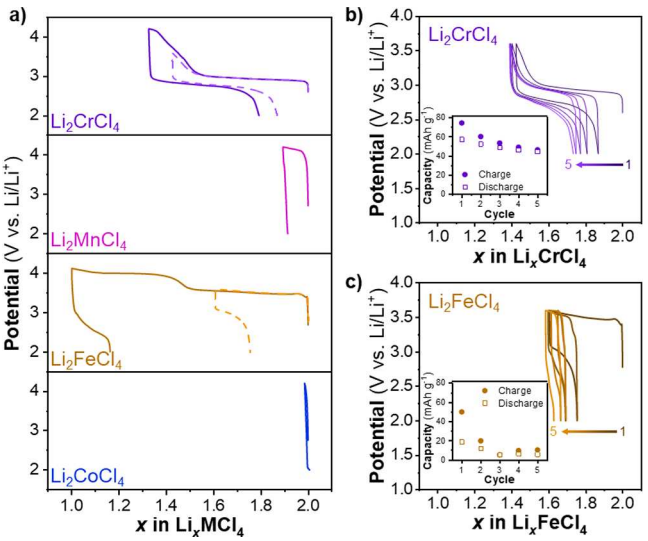

Figure 3. (a) Galvanostatic cycling of Li_2MCl_4 (M = Cr, Mn, Fe, Co) at 25 °C and a rate of C/10 in 5 M LiFSI in DMC. For Li_2CrCl_4 and Li_2FeCl_4, results obtained with cutoff potentials of 3.6 and 4.2 V vs Li/Li$^+$ are compared. Galvanostatic cycling of (b) Li_2CrCl_4 and (c) Li_2FeCl_4 (M = Cr Mn, Fe, Co) at 25 °C and a rate of C/10 in 5 M LiFSI in DMC with a cutoff potential of 3.6 V vs Li/Li$^+$. The charge and discharge capacities over the first 5 cycles are given in the inset.

activity of these compounds upon delithiation (Figure 3a). The results from galvanostatic cycling at a rate of C/10 at room temperature showed different behaviors as a function of the transition metal. For Mn- and Co-based halides, no reversible reaction was observed when cycling up to 4.2 V vs Li/Li$^+$. Li_2CrCl_4 and Li_2FeCl_4 showed two anodic events, a first one at potentials ∼3−3.5 V vs Li/Li$^+$ followed by a second one at potentials >4 V vs Li/Li$^+$. In situ XRD measurements confirmed that the first oxidation plateau is associated with the deinsertion of Li$^+$ from the Li_2MCl_4 structure, accom-

https://doi.org/10.1021/jacs.4c13005
J. Am. Chem. Soc. 2024, 146, 32059−32071

panied by a phase transformation indicated by the presence of new XRD peaks (Figure S1). Comparing results obtained with cutoff potentials of 3.6 V vs Li/Li$^+$ and 4.2 V vs Li/Li$^+$, one can conclude that the second oxidation event is irreversible for both compounds. For Li_2CrCl_4, the extra capacity observed in oxidation at high potentials is not recovered in reduction and thus likely originates from electrolyte oxidation, while the first redox plateau is found reversible. For Li_2FeCl_4, the oxidation at high potentials induces the loss of the Li$^+$ reinsertion plateau at around 3 V vs Li/Li$^+$. Altogether, these results suggest that Li_2FeCl_4 is decomposed at high potential, as previously observed for lithiated nitride phases $LiMoN_2$[48] for instance. This result is in line with previous reports for Li_2FeCl_4 using solid electrolytes where two similar oxidation events were observed, with the high potential one being fully irreversible while the low potential one shows very limited reversibility.[32−35,49] One can thus conclude that anodic decomposition occurs at high potentials and may be dependent on the electrolyte, possibly involving the reaction of oxidized Cl$^-$ ligands with DMC.[50] Nonetheless, capacities of 75 and 50 mAh/g were recorded for Li_2FeCl_4 and Li_2CrCl_4 upon the first charge using a cutoff voltage of 3.6 V vs Li/Li$^+$. Capacity losses corresponding to ∼35% and ∼80% of the initial capacity for Li_2CrCl_4 and Li_2FeCl_4, respectively, were recorded after only 5 cycles (Figure 3b,c), making these two phases of limited interest for practical applications under anodic/delithiation conditions.

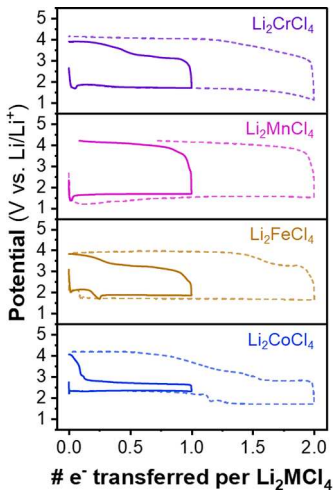

Figure 4. Galvanostatic cycling of Li_2MCl_4 (M = Cr, Mn, Fe, Co) at 55 °C and a rate of C/10 in 5 M LiFSI in DMC. Each material was cycled with a 1 e$^-$/f.u. limitation (solid line) and 2 e$^-$/f.u. limitation (dashed line).

We then turned our attention to the electrochemical behavior of each A_2MCl_4 phase during reduction. Figure 4 shows the galvanostatic cycling behavior of A_2MCl_4 (M = Cr, Mn, Fe, Co) with a rate of C/10 at 55 °C and limited to 1 and 2 e$^-$ per formula unit (f.u.). Initial reduction of Li_2MCl_4 where M = Cr, Mn, and Fe leads to a negative potential spike associated with a nucleation event followed by a single plateau at low potentials (<2 V vs Li/Li$^+$) for both the 1 e$^-$ and 2 e$^-$ transfer limit. Moreover, all three materials show very large hysteresis independent of the electron transfer limit. These features are characteristic of a conversion reaction, where (1) Li_nX (n being equal to the formal oxidation state of X) and metal nanoparticles nucleate and (2) poor electronic conductivity and bond breaking and reforming lead to large potential hysteresis.[17] Interestingly, Li_2CoCl_4 showed two plateaus in reduction. When the reduction was extended to 2 e$^-$/f.u., a large hysteresis was observed, similar to the conversion reaction observed for the other transition-metal halides. However, limiting the reaction to 1 e$^-$/f.u. led to a lower hysteresis (360 mV). Based on these results, we hypothesize that the 1 e$^-$ reaction of Li_2CoCl_4 follows a unique reaction path, different from the conversion-type behavior of Li_2MCl_4 where M = Cr, Mn, or Fe.

Prior to studying the physical and structural changes that occur during reduction, we further investigated the electrochemical behavior of the 1 e$^-$/f.u. redox reaction in Li_2CoCl_4. The results from extended galvanostatic cycling at 55 °C (Figure 5a) reveal that Li_2CoCl_4 delivers a reversible capacity of 125 mAh g^{-1} (1 e$^-$/f.u.) at C/10, close to the practical capacity of some intercalation materials such as $LiFePO_4$ (∼140−160 mAh g^{-1}).[51] The discharge and charge profiles of successive cycles perfectly overlap one another, maintaining the low potential hysteresis and demonstrating that the material is stable and does not suffer from dissolution, phase transformations, or other parasitic reactions. When cycled at a rate of C/10 in a controlled potential window between 2.2 and 3.2 V vs Li/Li$^+$, 84% capacity retention was observed after 15 cycles (Figure S2a,b). Increasing the charge/discharge rate to 1C (55 °C) leads to an increase in polarization and electrochemical grinding during the first several cycles before reaching a maximum capacity of ∼75 mAh g^{-1} (64% of the maximum capacity observed at C/10) (Figure S2c,d). The reversibility and capacity retention during cycling at higher rates support the hypothesis that the 1 e$^-$/f.u. reduction reaction in Li_2CoCl_4 is unique compared to the performance of conversion-type materials.

To gain further insight into the reactivity of Li_2CoCl_4, we investigated its electronic structure using first-principles calculations. As shown in Figure 6a, Li_2CoCl_4 is a pseudo one-dimensional system with weakly interacting $CoCl_6$ chains of edge-shared octahedra showing dispersive Co(d)-bands mainly along the M-R (c*-axis) direction of the Brillouin zone around the Fermi level. The local magnetic moment of cobalt is found to be $\mu_B \sim 2.7$, consistent with the high-spin d^7 configuration of Co(II). The Fukui functions f_+ and f_- show that the oxidation of Li_2CoCl_4 involves t_{2g}-like orbitals of Co(d_{xy}), making negligible δ-type Co−Co interactions along the chains (c-axis). Instead, its reduction involves other t_{2g}-like orbitals of Co(d_{xz}) making strong σ-type Co−Co interactions along the chains (Figure 6b). This may explain the inability to extract Li from this structure (no hole delocalization along the chains), while inserting Li is favorable (electron delocalization). Moreover, these results highlight the importance of the dimensionality of the MCl_6 linkages in determining the electrochemical reaction products. This contrasts with harsh chemical reduction reactions used to lithiate $CoCl_2$ and lithiated ternary compounds that leads to the formation of different metallic Co nanoparticle morphologies: reduction of $CoCl_2$ forms a nanoporous metal, while dilution of cobalt in Li_2CoCl_4 and Li_6CoCl_8 both lead to Co nanowire formation.[52,53]

Several reaction mechanisms must be considered during the reduction of Li_2CoCl_4, including an insertion reaction forming a Co(I) compound (eq 1a) followed by a conversion reaction (eq 1b); a displacement reaction forming metallic Co and a Li-

https://doi.org/10.1021/jacs.4c13005
J. Am. Chem. Soc. 2024, 146, 32059−32071

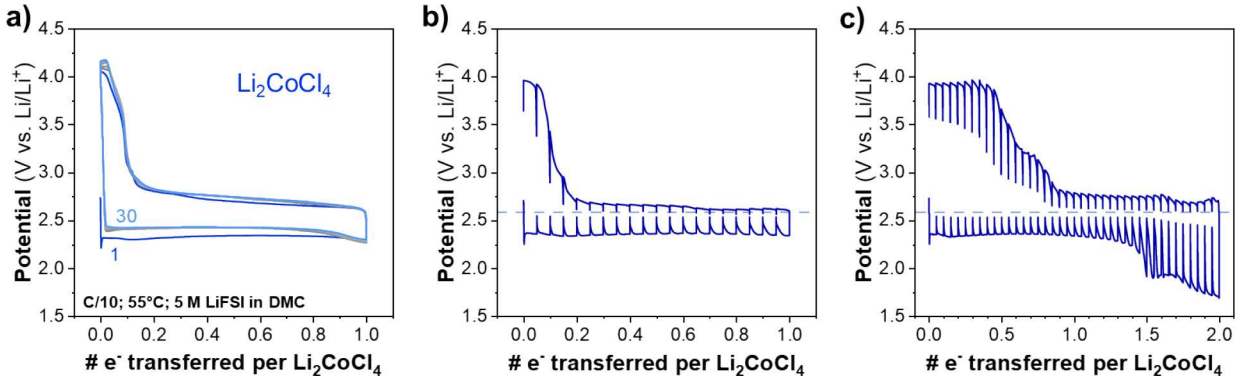

Figure 5. (a) Galvanostatic cycling of Li_2CoCl_4 at C/10 and 55 °C. Galvanostatic intermittent titration technique (GITT) results for Li_2CoCl_4 limited to the transfer of (b) 1 e^-/f.u. and (c) 2 e^-/f.u. The light blue dashed lines correspond to the $Co^{2+/0}$ redox potential.

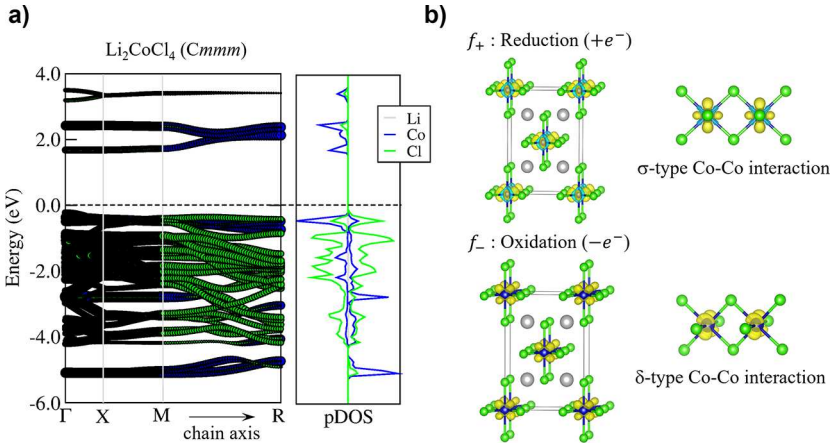

Figure 6. (a) Electronic band structure and atom-projected density of states (pDOS in arbitrary units) of the Li_2CoCl_4 structure in the C*mmm* space group computed with SCAN and showing a pseudo-1D electronic character along the chain direction. Γ, X, M, and R correspond to (0 0 0), (1/2 0 0), (1/2 1/2 0), and (1/2 1/2 1/2) k-point projections, respectively so that Γ→ X, X → M, and M→ R refer to the *a**, *b**, and *c** directions of the reciprocal lattice. (b) Fukui functions $f_+ = \rho(n+\varepsilon) - \rho(n)$ and $f_- = \rho(n) - \rho(n-\varepsilon)$ computed with SCAN for Li_2CoCl_4 showing the Co d-orbitals involved in the reduction and oxidation process, respectively. The yellow volumes stand for the additional charge density (negative for reduction and positive for the oxidation).

rich, Co-deficient intermediate phase (eq 2a) followed by conversion (eq 2b); a conversion reaction forming metallic Co and LiCl with morphological factors influencing the polarization (eq 3). Equation 2a represents a general case for the displacement reaction mechanism, whereby charge compensation for the Co(II) reduction is provided by Li^+ insertion in a topotactic reaction. It is also possible to undergo displacement reactions that (1) nucleate a thermodynamically stable phase that is Li-rich and TM-deficient, leading to a multiphase system that includes the pristine phase, displaced phase, and metallic nanoparticles at intermediate values of *x*, or (2) exchange one Li^+ for one TM with the remaining charge compensated by oxidizing transition metals in the original material.

$$Li_2CoCl_4 + Li^+ + e^- \rightarrow Li_3CoCl_4 \quad (1a)$$

$$Li_3CoCl_4 + Li^+ + e^- \rightarrow Co + 4LiCl \quad (1b)$$

$$Li_2CoCl_4 + xLi^+ + xe^- \rightarrow Li_{2+x}Co_{1-0.5x}Cl_4 + {}^1/_2xCo;\ 0 < x < 1 \quad (2a)$$

$${}^1/_2Li_6CoCl_8 + Li^+ + e^- \rightarrow {}^1/_2Co + 4LiCl \quad (2b)$$

$$Li_2CoCl_4 + 2Li^+ + 2e^- \rightarrow Co + 4LiCl \quad (3)$$

To discriminate between these different redox reactions, the galvanostatic intermittent titration technique (GITT) was used to reveal the equilibrium electrochemical potential of the material throughout reduction and oxidation. Figure 5b,c shows the GITT results for Li_2CoCl_4 cycled at C/20 and 55 °C with 0.05 e^- increments and 2 h rests at OCV between each step. When the GITT cycle was limited to 1 e^-/f.u. (Figure 5b), there was negligible hysteresis between the reduction plateau and the oxidation plateau. In the final stages of oxidation, the galvanostatic charging curve and the relaxation potential began to rise, which we attributed to some irreversibility in addition to electrolyte reactivity at potentials approaching 4 V vs Li/Li^+. The plateau voltage of 2.54 V vs Li/Li^+ aligns well with the expected reaction potential calculated for $Co^{2+/0}$ redox (2.59 V vs Li/Li^+; see Table S1 for thermodynamic data). Reducing Li_2CoCl_4 beyond 1 e^-/f.u. during GITT (Figure 5c) requires a larger activation for the reaction to proceed, thus leading to a higher polarization. However, the relaxation potential only very slightly changed from 2.54 V at 0.05 e^-/f.u. to 2.43 V at 1.95 e^-/f.u. Upon reoxidation, a polarization of ~140 mV is first observed after the exchange of 2 e^-, compared to only ~66 mV during the

https://doi.org/10.1021/jacs.4c13005
J. Am. Chem. Soc. 2024, 146, 32059−32071

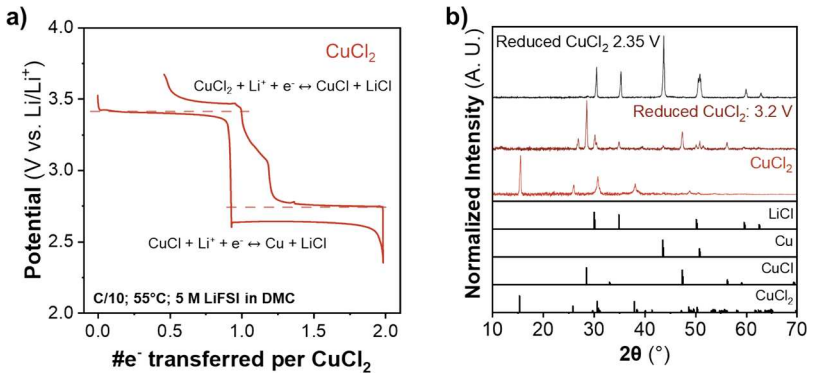

Figure 7. (a) Galvanostatic cycling of $CuCl_2$ at C/10 and 55 °C in 5 M LiFSI in DMC, and (b) in situ XRD patterns of $CuCl_2$ in the initial state and after the first and second reduction plateaus. The dashed lines in panel (a) represent the theoretical reduction potentials for the reactions shown in eqs 4 and 5.

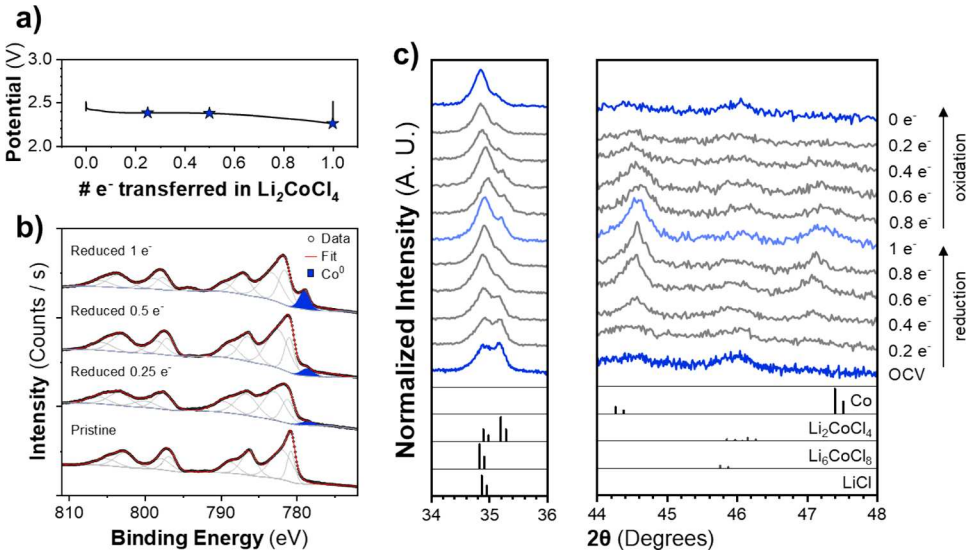

Figure 8. (a) Galvanostatic discharge curve and (b) ex situ X-ray photoelectron spectra of Li_2CoCl_4 at multiple degrees of reduction showing the emergence of Co(0) during the first reduction plateau. (c) In situ X-ray diffraction of Li_2CoCl_4 showing the emergence of HCP Co nanoparticles during reduction followed by subsequent disappearance during oxidation.

$1e^-$ reoxidation curve. At the end of the oxidation process, one new oxidation reaction pathway is recorded, showing high polarization and relaxation potentials in the range of 2.8−3.1 V vs Li/Li^+ followed by a high potential region ~3.8 V vs Li/Li^+ attributed to electrolyte reactivity (see discussion about anodic reactivity above). The conclusions from GITT results are that the reduction and oxidation reactions follow the same reaction path when the reduction is limited to 1 e^-/f.u., while extending the reduction to reach 2 e^-/f.u. shows similar relaxation potentials to the first plateau, attributed to the $Co^{2+/0}$ redox couple; however, this leads to large polarization and reaction path hysteresis upon reoxidation.

The electrochemical behavior of Li_2CoCl_4 is in stark contrast with that previously reported for layered transition metal halides such as VCl_3 or $CuCl_2$ (Figure 7).[30,54−56] Indeed, while VCl_3 was shown to undergo a classical intercalation process associated with the redox couple V^{3+}/V^{2+}, copper is known as one of the unique transition metals that can be stabilized as Cu(I), as in the CuCl structure. Hence, upon cycling $CuCl_2$ in 5 M LiFSI in DMC at 55 °C and a rate of C/10, two distinct reaction plateaus were observed, each corresponding to the transfer of 1 e^-/f.u. (Figure 7a), in agreement with prior reports.[17,55,56] The reduction plateaus at 3.40 and 2.67 V vs Li/Li^+ match the predicted potentials of two sequential 1 e^- conversion reactions (eqs 4 and 5; thermodynamic data provided in Table S1) shown by the dashed lines in Figure 7a and confirmed by in situ XRD (Figure 7b), which shows characteristic peaks of CuCl and LiCl.

$$CuCl_2 + Li^+ + e^- \rightarrow CuCl + LiCl\ (3.41V) \quad (4)$$

$$CuCl + Li^+ + e^- \rightarrow Cu + LiCl\ (2.74V) \quad (5)$$

Comparing the behavior of Li_2CoCl_4 to $CuCl_2$, it is clear that the two plateaus recorded in the reduction of Li_2CoCl_4 that show similar relaxation potentials cannot be explained by sequential Co^{2+}/Co^{1+} and Co^{1+}/Co^0 redox couples; thus, the low polarization plateau recorded during the first electron transfer in Li_2CoCl_4 is not associated with a Co^{2+}/Co^{1+} redox active couple. Overall, this comparison rules out insertion reaction mechanism (1).

To understand which mechanism is at play during the reactivity of Li_2CoCl_4 with Li, ex situ XPS experiments were carried out, focusing on the oxidation state of Co upon reduction using the core spectrum of the Co 2p region in the pristine material and after 0.25, 0.5, and 1 e^- reduction (Figure 8a,b). The spectrum of the pristine Li_2CoCl_4 shows two peaks

https://doi.org/10.1021/jacs.4c13005
J. Am. Chem. Soc. 2024, 146, 32059−32071

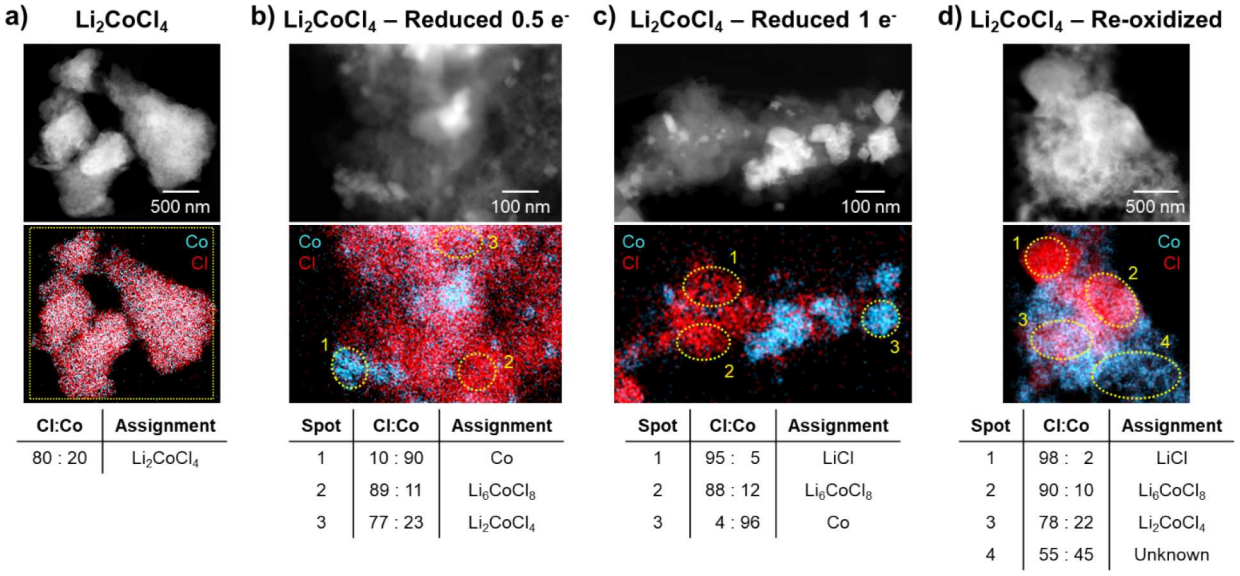

Cl:Co	Assignment
80 : 20	Li_2CoCl_4

Spot	Cl:Co	Assignment
1	10 : 90	Co
2	89 : 11	Li_6CoCl_8
3	77 : 23	Li_2CoCl_4

Spot	Cl:Co	Assignment
1	95 : 5	LiCl
2	88 : 12	Li_6CoCl_8
3	4 : 96	Co

Spot	Cl:Co	Assignment
1	98 : 2	LiCl
2	90 : 10	Li_6CoCl_8
3	78 : 22	Li_2CoCl_4
4	55 : 45	Unknown

Figure 9. Ex situ STEM HAADF images with EDS mapping quantifying the cobalt and chlorine ratio in (a) pristine Li_2CoCl_4, (b) Li_2CoCl_4 reduced by 0.5 e^-/f.u., (c) Li_2CoCl_4 reduced by 1 e^-/f.u., and (d) Li_2CoCl_4 that was reduced by 0.5 e^-/f.u. and reoxidized to 3 V.

corresponding to the $2p_{3/2}$ and $2p_{1/2}$ transitions at 780.9 and 797.2 eV, respectively, ascribed to Co(II). The peaks positioned at a higher binding energy compared to the $2p_{3/2}$ and $2p_{1/2}$ peaks are the respective satellite peaks. The Co(II) signature was observed at all stages of reduction, as expected based on the reaction mechanisms in eqs 2 and 3. However, a peak at 779 eV (highlighted in blue) corresponding to Co(0) emerged in the reduced samples as early as 0.25 e^-/f.u. The intensity of the Co(0) peak increases with the degree of reduction from 0.25 to 1 e^-/f.u. The results from ex situ XPS provide direct evidence that the electrochemical mechanism during the first reduction plateau of Li_2CoCl_4 involves the $Co^{2+/0}$ redox couple, therefore ruling out the possible formation of a Co(I) compound as required by eq 1a.

To differentiate between the displacement (eq 2a) and conversion reactions (eq 3), in situ X-ray diffraction measurements were carried out during the first reduction and reoxidation (Figure 8c). Peaks at 44.57° and 47.13° were observed upon reduction, and their peak intensities increased during reduction and decreased during oxidation. These peaks are attributed to the reversible formation/consumption of Co nanoparticles, in agreement with the results from XPS. During reduction, the intensity of the (201) peak of Li_2CoCl_4 at 35.18° decreases, but does not completely disappear, suggesting that a small amount of Li_2CoCl_4 is retained after 1 e^- reduction. This peak does not completely disappear until full reduction is reached, after which only peaks associated with LiCl and Co nanoparticles are observed (Figure S3). A peak at 34.91° is found to increase in intensity during reduction. This peak can be associated with the formation of either Li_6CoCl_8 or LiCl. Nevertheless, these three compounds, Li_2CoCl_4, LiCl, and Li_6CoCl_8, share a similar anionic framework, with only slight differences in the cationic occupation of interstitial sites. As a result, their diffraction peaks, for both X-ray and electron diffraction, overlap (Figure S4).

Due to the overlapping diffraction patterns of the pristine and reduced phases, STEM imaging coupled with EDS analysis was carried out to quantify the composition of Cl and Co in the phases present at different states of charge (Figure 9). Since chlorides are known to be beam sensitive, extra care was taken to ensure that the observations of pristine and ex situ Li_2CoCl_4 samples were not a result of beam damage (additional EDS data and discussion regarding sample stability are provided in Figure S5 and Supplemental Note 1). EDS mapping of pristine Li_2CoCl_4 (Figure 9a) reveals that Co and Cl are uniformly distributed throughout large micrometer scale particles, with the expected Cl:Co ratio of 4:1. After a reduction corresponding to the exchange of 0.5 e^-/f.u., residual pristine Li_2CoCl_4 with Cl:Co of 4:1 was observed in addition to Co nanoparticles and Co-deficient, Cl-rich regions with Cl:Co close to 8:1 (Figure 9b). This result provides evidence that the reduction process proceeds through a displacement reaction involving the formation of a Li_6CoCl_8 intermediate, along with Co nanoparticles. This conclusion is reinforced by observing that for a sample that underwent reduction to 1 e^-/f.u., Li_2CoCl_4 was no longer observed and regions of Co and Li_6CoCl_8 were once again present (Figure 9c). Nevertheless, regions of LiCl are also observed after 1 e^- reduction, indicating that the onset of the conversion reaction is concomitant with the end of the displacement reaction. This observation is consistent with electrochemical results that show a variable onset of the conversion reaction between 0.8 and 1.2 e^-/f.u for cells cycled under identical conditions (Figure S8). This indicates that the displacement reaction is highly sensitive to packing density, local current density, and polarization, among other parameters, which can eventually be optimized by the use of coated electrodes or by controlling the cell pressure. The results from reoxidation of a sample reduced to 0.5 e^-/f.u. (Figure 9d) are difficult to interpret due to the possible presence of unreacted material after the partial discharge and charging to only 3 V. However, no cobalt nanoparticles were observed, which confirms that the reversible reaction involves the reoxidation of Co nanoparticles.

The formation of cobalt nanoparticles and the cobalt-deficient phase, Li_6CoCl_8, observed via STEM/EDS, provides evidence that the reduction of Li_2CoCl_4 follows the displacement reaction (eq 2a). Unlike conversion that is well-known to suffer from large polarization associated with the energy barrier to break and form metal−ligand and lithium-ligand bonds,[17,57,58] the displacement reaction mechanism exhibits

https://doi.org/10.1021/jacs.4c13005
J. Am. Chem. Soc. 2024, 146, 32059−32071

low hysteresis,[59] while the polarization progressively increases from 1 to 2 e^- transferred per formula unit when the reaction mechanism switches to conversion. As for any displacement reaction, there is a topotactic exchange of the inserted cations with the TM that is removed from the structure upon reduction. Hence, the displacement reaction is enabled by the structural similarities existing between the initial and the final

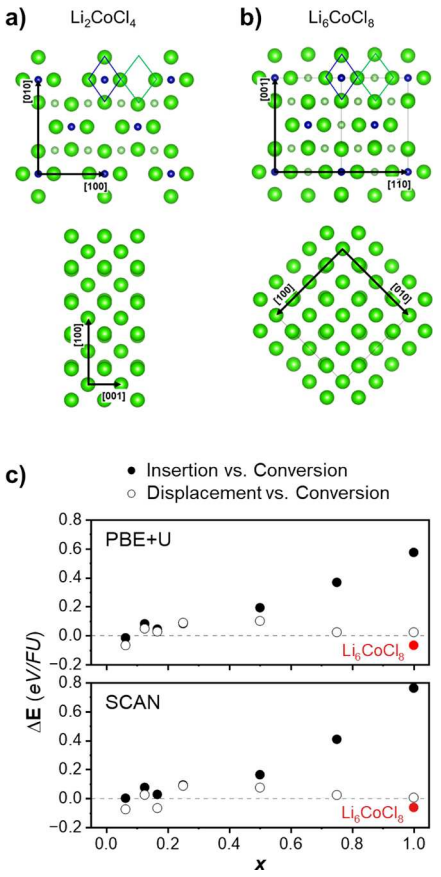

Figure 10. Crystal structures of (a) Li_2CoCl_4 and (b) Li_6CoCl_8 showing the similar anion sublattice in each material. (c) Phase stability diagrams for the insertion and displacement reactions (both compared to the direct conversion of Li_2CoCl_4 into Co(0) + 4LiCl) as computed from DFT+U and SCAN. The Li_6CoCl_8 phase is indicated in red at $x = 1$.

product, i.e., between the chloride anion lattice in Li_2CoCl_4 and Li_6CoCl_8, shown in Figure 10a,b. Indeed, in Li_2CoCl_4, $CoCl_6$ octahedra have Cl−Co−Cl distances of 4.926 and 4.934 Å and Cl−Li−Cl distances of 5.101 and 5.145 Å. In Li_6CoCl_8, similar distances are observed, with Cl−Co−Cl distances of 4.890 Å and Cl−Li−Cl distances of 5.155 Å. Thus, no major volume expansion is observed during the displacement. However, the electrochemical transition from Li_2CoCl_4 to Li_6CoCl_8 requires mild thermal activation at 55 °C. Figure S9 shows that during the reduction of Li_2CoCl_4 at room temperature only the plateau at 1.7 V is observed, and the low polarization plateau associated with the displacement reaction is not observed. The extra capacity that is observed during reduction to potentials below ∼1.7 V includes the reactivity of the electrolyte, as confirmed by cycling a cell with conductive carbon as the electrode (Figure S10). The structural similarities provided by the anion lattice allow for topotactic cation exchange of 2 Li^+ and 1 Co(II) ion during the displacement reaction upon mild thermal activation at 55 °C, indicating either some kinetics limitation due to hindered Co or Li diffusion in the defective structure, or a slightly more positive Gibbs free energy for the formation of Li_6CoCl_8 when compared to the formation of Co(0) and LiCl.

First-principles DFT+U calculations were carried out to further understand the energy landscape of the insertion, displacement, and conversion reaction mechanisms during the lithiation of Li_2CoCl_4. Note that a partial displacement reaction resulting in the oxidation of some Co(II) to Co(III) upon exchanging one Li^+ and one Co(II) was not considered here, as this reaction was supported neither by our XPS results nor by the existence of a Co(III) containing lithium cobalt chloride phase in crystallographic databases. As shown in Figure 10c, both insertion and displacement reactions compete with the conversion reaction at the very beginning of discharge ($x < 0.25$). Above this critical value, the insertion reaction becomes very unfavorable (in agreement with the undesired Co(II) reduction to Co(I)) while the displacement reaction appears very close in energy to the conversion reaction. Following the convex hull of this phase stability diagram, the formation of $1/2Li_6CoCl_8 + 1/2Co$ (red data point in Figure 10c) following a multiphase displacement reaction is thermodynamically favored over conversion in the composition range from $x = 0$ (Li_2CoCl_4) to 1 ($1/2Li_6CoCl_8 + 1/2Co$). Similar conclusions were drawn using DFT+U and SCAN methods, thus revealing that a multiphase displacement reaction is thermodynamically feasible upon reduction for Li_2CoCl_4, in agreement with the experimental observations discussed above. Furthermore, based on the computational results, one can conclude that the requirement for thermal activation originates from kinetic limitations of Li and/or Co diffusion rather than unfavorable Gibbs free energy of formation at low temperature. The displacement reaction stops when Li^+ cations alternatively occupy half of the Co(II) sites along the 1D octahedral chains. One can hypothesize that within this configuration, the diffusion pathway for the displacement of Co(II) is inhibited and/or the electronic conductivity is severely limited by the transition from 1D chains of $CoCl_6$ octahedra forming Co−Co chains with electronic delocalization to isolated 0D $CoCl_6$. However, more remains to be done to better comprehend diffusion and electronic properties of this phase at different lithiation stages.

To further understand the reactivity of the Li_2CoCl_4−Li_6CoCl_8−LiCl system, we synthesized the cobalt-deficient defect-rock salt intermediate phase, Li_6CoCl_8. XRD results shown in Figure S11 confirm the formation of the $Fm\bar{3}m$ structure reported by Kanno et al.[60] Pristine Li_6CoCl_8 was cycled in 5 M LiFSI in DMC at 55 °C and a rate of C/10 with the discharge limited to 0.5, 1, and 2 e^-/f.u. of Li_6CoCl_8 (Figure S12a). The results show that ∼0.5 e^-/f.u. is reversibly cycled, while further reduction leads to an increase in polarization and reduction potentials that overlap with electrolyte decomposition, thus leading to irreversibility and large voltage hysteresis. During the reduction of Li_6CoCl_8, a large feature is observed at the early stages, characteristic of a nucleation event during a conversion reaction, that is followed by a sloping discharge curve with a continuously increasing polarization. In short, the electrochemical behavior of Li_6CoCl_8 during reduction matches that observed for Li_2CoCl_4 when more than 1 e^-/f.u. is exchanged. Oxidation leads to a sloping voltage profile between 2.55 and 2.81 V vs Li/Li^+ that recovers 83% of the discharge capacity before a steep increase in the

https://doi.org/10.1021/jacs.4c13005
J. Am. Chem. Soc. 2024, 146, 32059−32071

potential. When comparing the results of Li_2CoCl_4 and Li_6CoCl_8, the latter shows larger hysteresis (490 mV compared to 360 mV in Li_2CoCl_4), one narrow and one large nucleation event at the beginning of discharge, and a constantly increasing polarization during discharge. Conversely, Li_2CoCl_4 shows one narrow nucleation event at the very beginning of the discharge and a distinct voltage plateau. Next, we performed the galvanostatic intermittent titration technique on Li_6CoCl_8, which showed that only ~0.2 e^-/f.u. could be exchanged during the first reduction event before quickly transitioning to a low voltage region (<2 V vs Li/Li^+) that involves the competition between continued conversion of the pristine material and decomposition of the electrolyte (Figure S12b). Ultimately, these results show that reversible Li-ion reactivity with Li_6CoCl_8 is limited to only 0.5 e^-/f.u. or about 1/4 of the cobalt that remains from the initial Li_2CoCl_4 structure. We hypothesize that this is related to the 0-D structure formed in Li_6CoCl_8 with isolated $CoCl_6$ octahedra, thus impeding cobalt and electron transport.

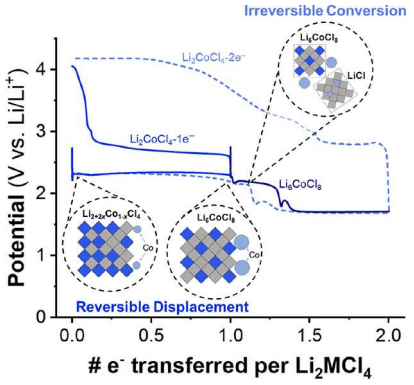

Figure 11. Proposed reaction mechanism of the electrochemical reactivity of Li_2CoCl_4 with lithium.

Considering together the reactivity of Li_2CoCl_4 and Li_6CoCl_8, the reduction mechanism of Li_2CoCl_4 is proposed to go through the following stages (Figure 11): (i) the displacement reaction of Li_2CoCl_4 represented by a low polarization plateau that forms 1/2Co and $1/2Li_6CoCl_8$, (ii) an additional nucleation event at moderate overpotentials representing the reactivity of Li_6CoCl_8 followed by a steady increase in polarization that is limited to ~$1/4e^-$/f.u., and (iii) a low potential nucleation event and plateau attributed to the competing conversion reaction and electrolyte decomposition. Plotted together (Figure 11 and Figure S13), the voltage profiles match well with each other and resemble the full reduction of Li_2CoCl_4, with some deviation expected based on the complex evolution of the electrochemical interfaces and morphology during the in situ formation of the Li_6CoCl_8 intermediate (consistent with the observation of some variability in the onset of the transition region after the first reduction plateau). These results provide strong evidence supporting the displacement reaction of Li_2CoCl_4 leading to the formation of the Li_6CoCl_8 intermediate phase.

By comparing several alkali transition metal chlorides with the same stoichiometry and different structures, our study reveals the following criteria that determine whether a displacement reaction can occur in ternary Li-TM-Cl compounds: (1) the original structure must contain 1D chains of edge-sharing octahedra that favor electronic delocalization and (2) a transition-metal-deficient intermediate must be available with the same TM oxidation state. Criterion 1 is supported by comparing Li_2FeCl_4 and Li_2CoCl_4. For Li_2FeCl_4, an intermediate structure has been reported, Li_6FeCl_8. However, the pristine phase forms a 3D interconnected structure. We hypothesize that the distribution of Fe(II) and Li^+ throughout the inverse spinel structure blocks diffusion pathways for each cation into and out of the structure, thus leading to a high polarization. Criterion 2 is supported by comparing Li_2CrCl_4 and Li_2CoCl_4. In Li_2CrCl_4, the pristine structure contains 1D chains of edge-sharing octahedra along the [001] direction; however, the only transition-metal-deficient phase reported contains Cr(III), which is not expected to form during the reduction from Cr(II).

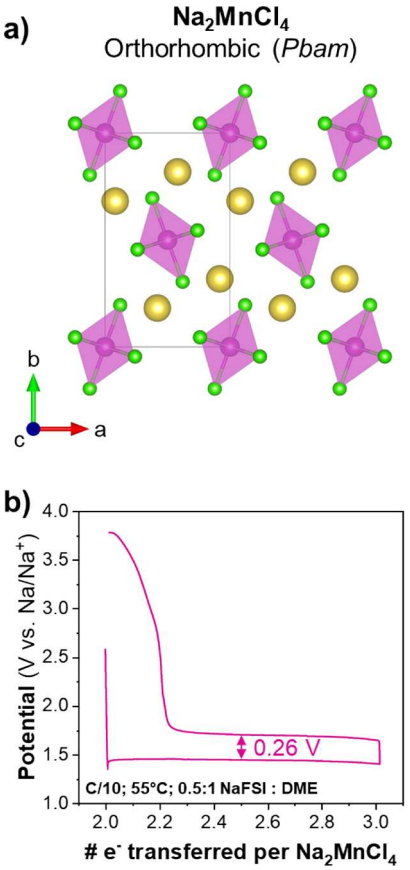

Figure 12. (a) Crystal structure of Na_2MnCl_4 and (b) galvanostatic cycling of Na_2MnCl_4 in a high concentration Na-ion electrolyte consisting of a 0.5:1 molar ratio of NaFSI:DME.

To test the universality of these design principles, we screened several compounds (Table S2). Doing so, we found that Na_2MnCl_4 forms a structure with 1D chains of edge-sharing octahedra (Figure 12a) and has a reported transition metal-deficient structure with Mn(II) cations, Na_6MnCl_8.[61,62] Na_2MnCl_4 was thus synthesized following a similar mechanochemical synthetic route, and its electrochemical reactivity was tested in a high concentration of Na-ion electrolyte containing a 0.5:1 molar ratio of NaFSI:DME. Figure 12b shows the galvanostatic cycling performance of Na_2MnCl_4 at a rate of C/10 and at 55 °C. During the first cycle, we observed a reversible low polarization plateau when limited to 1 e^-/f.u.

https://doi.org/10.1021/jacs.4c13005
J. Am. Chem. Soc. 2024, 146, 32059−32071

The total potential hysteresis between discharge and charge was 0.26 V, which is lower than that of Li_2CoCl_4. The electrochemical behavior observed for Na_2MnCl_4 is characteristic of the displacement reaction, thus validating the proposed criteria for both Na-ion and Li-ion containing A_2MCl_4 phases and showing that these can be used to design novel halide-based materials reacting with either Li or Na following a reversible, low polarization displacement reaction. However, limited stability was observed upon cycling, calling for a deeper analysis of the dissolution mechanism in Na-based highly concentrated electrolytes and the electrochemical stability window of the high-concentration Na-ion electrolytes.

4. CONCLUSIONS

In this work, we investigated for the first time the electrochemical reactivity of ternary transition-metal chlorides with A_2MCl_4 stoichiometry using liquid electrolytes. By using high-concentration electrolytes, we demonstrate that the dissolution of halide compounds is suppressed, allowing for studying their reactivity with lithium. By comparing the galvanostatic cycling behavior of 4 compounds (Li_2MCl_4; M = Cr, Mn, Fe, Co) in 5 M LiFSI in DMC, we found, to no surprise, that they all undergo a conversion reaction when reacting with 2 Li^+ and 2 e^-. However, Li_2CoCl_4 displays a significantly lower polarization between the reduction and oxidation reactions compared to the other compounds when reduction was limited to 1 e^-/f.u., indicating a different reaction mechanism than conversion. During the low polarization plateau, cobalt nanoparticles are formed, as confirmed by in situ XRD, ex situ XPS, and ex situ STEM/EDS. While this could indicate a conversion reaction, results from ex situ EDS provide evidence of the formation of the Li_6CoCl_8 intermediate, consistent with the thermodynamically favorable path predicted by DFT calculations for a displacement reaction. Unlike a conversion reaction for which bonds are broken and reformed during the reaction, the displacement reaction is a topotactic reaction that shows a low polarization during galvanostatic cycling when the cationic diffusion is assisted by temperature. By comparing Li_2CoCl_4 to the Cr, Mn, and Fe-containing compounds, we determined that ternary alkali transition-metal chlorides must meet the following criteria to undergo an electrochemical displacement reaction: (1) contain 1D chains of edge-sharing octahedra to favor electronic delocalization and (2) have an available transition metal-deficient phase, such as the A_6MCl_8 intermediate. We further validated the universality of these design criteria by screening several compounds. Doing so, we demonstrated that Na_2MnCl_4, which fulfills all of these criteria, undergoes a reversible electrochemical reaction characterized by a low polarization reduction reaction similar to Li_2CoCl_4. This outcome reveals that the structure−reactivity relationships developed in this study apply to Li-ion and Na-ion systems. Overall, this work sheds light on a new family of electrochemically active alkali transition-metal chlorides and reveals the underlying structural factors that lead to a low polarization displacement reaction in chloride compounds. This work motivates further studies to determine whether these structure−reactivity relationships can be extended to compounds with oxide, sulfide, and fluoride ligands containing 1D structural features. Moreover, the similar anion lattices of pristine and intermediate phases are advantageous for reversible, topotactic reactions; however, they present challenges in characterizing the structural evolution of materials during reaction with lithium. Thus, characterization of the ternary chlorides and other compounds is required using advanced techniques such as operando synchrotron X-ray diffraction with a variable temperature stage and electron diffraction analyzed using a charge-flipping method similar to what has been done for the FeF_3 system,[20] provided that the phases can be stabilized, to definitively observe intermediate structures formed during topotactic electrochemical displacement reactions.

■ ASSOCIATED CONTENT

Supporting Information

The Supporting Information is available free of charge at https://pubs.acs.org/doi/10.1021/jacs.4c13005.

In-situ and ex-situ X-ray diffraction patterns; simulated X-ray and electronic diffraction patterns; thermodynamic tables; Galvanostatic cycling curves; transmission electron microscopy analysis and discussion (PDF)

■ AUTHOR INFORMATION

Corresponding Author

Alexis Grimaud − *Department of Chemistry, Boston College, Chestnut Hill, Massachusetts 02467, United States;* orcid.org/0000-0002-9966-205X; Email: alexis.grimaud@bc.edu

Authors

Michael A. Spencer − *Department of Chemistry, Boston College, Chestnut Hill, Massachusetts 02467, United States;* orcid.org/0000-0002-9552-2842

Tae Gyu Yun − *Department of Chemistry, Boston College, Chestnut Hill, Massachusetts 02467, United States;* orcid.org/0000-0002-6335-2893

Marguerite Flynn − *Department of Chemistry, Boston College, Chestnut Hill, Massachusetts 02467, United States*

Marie-Liesse Doublet − *Réseau sur le Stockage Électrochimique de l'Énergie (RS2E), CNRS, Amiens 80039, France; ICGM, Univ Montpellier, CNRS, ENSCM, Montpellier 34095, France;* orcid.org/0000-0002-8495-2716

Complete contact information is available at: https://pubs.acs.org/10.1021/jacs.4c13005

Notes

The authors declare no competing financial interest.

■ ACKNOWLEDGMENTS

This material is based upon work supported by the National Science Foundation under Award No. DMR-2326843. The authors would like to acknowledge the Boston College Materials Characterization Core and MIT. Nano for facilitating some of the work presented in this publication.

■ REFERENCES

(1) Manthiram, A. A Reflection on Lithium-Ion Battery Cathode Chemistry. *Nat. Commun.* **2020**, *11* (1), 1550.

(2) Whittingham, M. S. Electrical Energy Storage and Intercalation Chemistry. *Science* **1976**, *192* (4244), 1126−1127.

(3) Whittingham, M. S. The Hydrated Intercalation Complexes of the Layered Disulfides. *Mater. Res. Bull.* **1974**, *9*, 1681−1690.

(4) Whittingham, M. S. The Role of Ternary Phases in Cathode Reactions. *J. Electrochem. Soc.* **1976**, *123* (3), 315−320.

(5) Whittingham, M. S.; Gamble, F. R. The Lithium Intercalates of the Transition Metal Dichalcogenides. *Mater. Res. Bull.* **1975**, *10* (5), 363−371.
(6) Mizushima, K.; Jones, P. C.; Wiseman, P. J.; Goodenough, J. B. Li_xCoO_2 ($0 < X \leq 1$): A New Cathode Material for Batteries of High Energy Density. *Mater. Res. Bull.* **1980**, *15* (6), 783−789.
(7) Thackeray, M. M.; David, W. I. F.; Bruce, P. G.; Goodenough, J. B. Lithium Insertion into Manganese Spinels. *Mater. Res. Bull.* **1983**, *18* (4), 461−472.
(8) Goodenough, J. B. Evolution of Strategies for Modern Rechargeable Batteries. *Acc. Chem. Res.* **2013**, *46* (5), 1053−1061.
(9) Delmas, C.; Carlier, D.; Guignard, M. The Layered Oxides in Lithium and Sodium-Ion Batteries: A Solid-State Chemistry Approach. *Adv. Energy Mater.* **2021**, *11* (2), 2001201.
(10) Bruce, P. G.; Scrosati, B.; Tarascon, J. Nanomaterials for Rechargeable Lithium Batteries. *Angew. Chem., Int. Ed.* **2008**, *47* (16), 2930−2946.
(11) Palacín, M. R.; Simon, P.; Tarascon, J. M. Nanomaterials for Electrochemical Energy Storage: The Good and the Bad. *Acta Chim Slov* **2016**, *63* (3), 417−423.
(12) Poizot, P.; Laruelle, S.; Grugeon, S.; Dupont, L.; Tarascon, J.-M. Nano-Sized Transition-Metal Oxides as Negative-Electrode Materials for Lithium-Ion Batteries. *Nature* **2000**, *407* (6803), 496−499.
(13) Morcrette, M.; Rozier, P.; Dupont, L.; Mugnier, E.; Sannier, L.; Galy, J.; Tarascon, J. M. A Reversible Copper Extrusion-Insertion Electrode for Rechargeable Li Batteries. *Nat. Mater.* **2003**, *2* (11), 755−761.
(14) Obrovac, M. N.; Dunlap, R. A.; Sanderson, R. J.; Dahn, J. R. The Electrochemical Displacement Reaction of Lithium with Metal Oxides. *J. Electrochem. Soc.* **2001**, *148* (6), A576.
(15) Xiao, A. W.; Lee, H. J.; Capone, I.; Robertson, A.; Wi, T. U.; Fawdon, J.; Wheeler, S.; Lee, H. W.; Grobert, N.; Pasta, M. Understanding the Conversion Mechanism and Performance of Monodisperse FeF_2 Nanocrystal Cathodes. *Nat. Mater.* **2020**, *19* (6), 644−654.
(16) Li, T.; Li, L.; Cao, Y. L.; Ai, X. P.; Yang, H. X. Reversible Three-Electron Redox Behaviors of FeF_3 Nanocrystals as High-Capacity Cathode-Active Materials for Li-Ion Batteries. *J. Phys. Chem. C* **2010**, *114* (7), 3190−3195.
(17) Cabana, J.; Monconduit, L.; Larcher, D.; Palacín, M. R. Beyond Intercalation-Based Li-Ion Batteries: The State of the Art and Challenges of Electrode Materials Reacting through Conversion Reactions. *Adv. Mater.* **2010**, *22* (35), E170.
(18) Nitta, N.; Wu, F.; Lee, J. T.; Yushin, G. Li-Ion Battery Materials: Present and Future. *Mater. Today* **2015**, *18* (5), 252−264.
(19) Pralong, V.; Souza, D. C. S.; Leung, K. T.; Nazar, L. F. Reversible Lithium Uptake by CoP_3 at Low Potential: Role of the Anion. *Electrochem commun* **2002**, *4* (6), 516−520.
(20) Hua, X.; Eggeman, A. S.; Castillo-Martínez, E.; Robert, R.; Geddes, H. S.; Lu, Z.; Pickard, C. J.; Meng, W.; Wiaderek, K. M.; Pereira, N.; Amatucci, G. G.; Midgley, P. A.; Chapman, K. W.; Steiner, U.; Goodwin, A. L.; Grey, C. P. Revisiting Metal Fluorides as Lithium-Ion Battery Cathodes. *Nat. Mater.* **2021**, *20* (6), 841−850.
(21) Boyanov, S.; Bernardi, J.; Gillot, F.; Dupont, L.; Womes, M.; Tarascon, J.-M.; Monconduit, L.; Doublet, M.-L. FeP: Another Attractive Anode for the Li-Ion Battery Enlisting a Reversible Two-Step Insertion/Conversion Process. *Chem. Mater.* **2006**, *18* (15), 3531−3538.
(22) Gillot, F.; Bichat, M. P.; Favier, F.; Morcrette, M.; Doublet, M. L.; Monconduit, L. The Li_xMPn_4 Phases (M/Pn = Ti/P, V/As): New Negative Electrode Materials for Lithium Ion Rechargeable Batteries. *Electrochim. Acta* **2004**, *49* (14), 2325−2332.
(23) Monconduit, L.; Gillot, F.; Doublet, M.-L.; Lemoigno, F. Lithium Insertion/Deinsertion Mechanisms in the Transition Metal Pnictides Li_xMPn_4. *Ionics* **2003**, *9* (1−2), 56−63.
(24) Souza, D. C. S.; Pralong, V.; Jacobson, A. J.; Nazar, L. F. A Reversible Solid-State Crystalline Transformation in a Metal Phosphide Induced by Redox Chemistry. *Science* **2002**, *296*, 2012−2015.
(25) Nishijima, M.; Takeda, Y.; Imanishi, N.; Yamamoto, O.; Takano, M. Li Deintercalation and Structural Change in the Lithium Transition Metal Nitride Li_3FeN_2. *J. Solid State Chem.* **1994**, *113* (1), 205−210.
(26) Nishijima, M.; Tadokoro, N.; Takeda, Y.; Imanishi, N.; Yamamoto, O. Li Deintercalation-Intercalation Reaction and Structural Change in Lithium Transition Metal Nitride, Li_7MnN_4. *J. Electrochem. Soc.* **1994**, *141* (11), 2966−2971.
(27) Suzuki, S. Electronic Structure and Electrochemical Properties of Electrode Material $Li_{7-x}MnN_4$. *Solid State Ion* **1999**, *116* (1−2), 1−9.
(28) Zhan, X.; Li, M. M.; Weller, J. M.; Sprenkle, V. L.; Li, G. Recent Progress in Cathode Materials for Sodium-Metal Halide Batteries. *Materials* **2021**, *14* (12), 3260.
(29) Dai, Y.; Zhang, S.; Wen, J.; Song, Z.; Wang, T.; Zhang, R.; Fan, X.; Luo, W. Metal Chloride Cathodes for Next-Generation Rechargeable Lithium Batteries. *iScience* **2024**, *27* (4), No. 109557.
(30) Dubouis, N.; Marchandier, T.; Rousse, G.; Marchini, F.; Fauth, F.; Avdeev, M.; Iadecola, A.; Porcheron, B.; Deschamps, M.; Tarascon, J. M.; Grimaud, A. Extending Insertion Electrochemistry to Soluble Layered Halides with Superconcentrated Electrolytes. *Nat. Mater.* **2021**, *20* (11), 1545−1550.
(31) He, B.; Zhang, F.; Xin, Y.; Xu, C.; Hu, X.; Wu, X.; Yang, Y.; Tian, H. Halogen Chemistry of Solid Electrolytes in All-Solid-State Batteries. *Nat. Rev. Chem.* **2023**, *7* (12), 826−842.
(32) Kajiyama, A.; Takada, K.; Inada, T.; Kouguchi, M.; Kondo, S.; Watanabe, M.; Tabuchi, M. Electrochemical Deintercalation of Lithium Ions from Lithium Iron Chloride Spinel. *Solid State Ion* **2002**, *152−153*, 295−302.
(33) Tanibata, N.; Kato, M.; Takimoto, S.; Takeda, H.; Nakayama, M.; Sumi, H. High Formability and Fast Lithium Diffusivity in Metastable Spinel Chloride for Rechargeable All-Solid-State Lithium-Ion Batteries. *Advanced Energy and Sustainability Research* **2020**, *1* (1), 2000025.
(34) Tanibata, N.; Takimoto, S.; Aizu, S.; Takeda, H.; Nakayama, M. Applying the HSAB Design Principle to the 3.5 V-Class All-Solid-State Li-Ion Batteries with a Chloride Electrolyte. *J. Mater. Chem. A Mater.* **2022**, *10* (39), 20756−20760.
(35) Hao, J.; Ma, C. A Deformable Spinel-Type Chloride Cathode with High Ionic Conductivity for All-Solid-State Li Batteries. *Journal of University of Science and Technology of China* **2022**, *52* (12), 4.
(36) Rodriguez-Carvajal, J.FULLPROF: A Program for Rietveld Refinement and Pattern Matching Analysis. *Abstracts of the Satellite Meeting on Powder Diffraction of the XV Congress of the IUCr*; Laboratoire Léon Brillouin (CEA−CNRS) 1990, *127*.
(37) Momma, K.; Izumi, F. *VESTA 3* for Three-Dimensional Visualization of Crystal, Volumetric and Morphology Data. *J. Appl. Crystallogr.* **2011**, *44* (6), 1272−1276.
(38) Kresse, G.; Furthmüller, J. Efficiency of Ab-Initio Total Energy Calculations for Metals and Semiconductors Using a Plane-Wave Basis Set. *Comput. Mater. Sci.* **1996**, *6* (1), 15−50.
(39) Kresse, G.; Joubert, D. From Ultrasoft Pseudopotentials to the Projector Augmented-Wave Method. *Phys. Rev. B* **1999**, *59* (3), 1758−1775.
(40) Blöchl, P. E. Projector Augmented-Wave Method. *Phys. Rev. B* **1994**, *50* (24), 17953−17979.
(41) Perdew, J. P.; Burke, K.; Ernzerhof, M. Generalized Gradient Approximation Made Simple. *Phys. Rev. Lett.* **1996**, *77* (18), 3865−3868.
(42) Dudarev, S. L.; Botton, G. A.; Savrasov, S. Y.; Humphreys, C. J.; Sutton, A. P. Electron-Energy-Loss Spectra and the Structural Stability of Nickel Oxide: An LSDA+U Study. *Phys. Rev. B* **1998**, *57* (3), 1505−1509.
(43) Sun, J.; Ruzsinszky, A.; Perdew, J. P. Strongly Constrained and Appropriately Normed Semilocal Density Functional. *Phys. Rev. Lett.* **2015**, *115* (3), No. 036402.

https://doi.org/10.1021/jacs.4c13005
J. Am. Chem. Soc. 2024, 146, 32059−32071

(44) Lutz, H. D.; Schneider, M.; Wickel, C. Neutron Powder Diffraction on Monoclinic Li_2CrCl_4. *Z. Kristallogr Cryst. Mater.* **1996**, *211* (1), 8−12.
(45) Lutz, H. D.; Schneider, M. Kristallstruktur Des Li_2MnCl_4/ The Crystal Structure of Li_2MnCl_4. *Zeitschrift für Naturforschung B* **1990**, *45* (11), 1543−1547.
(46) Lutz, H. D.; Pfitzner, A.; Cockcroft, J. K. Structural Phase Transition and Nonstoichiometry of Li_2FeCl_4—Neutron Diffraction Studies. *J. Solid State Chem.* **1993**, *107* (1), 245−249.
(47) Schneider, M.; Lutz, H. D.; Cockcroft, J. K. Polymorphie Und Pseudosymmetrie von Li_2CoCl_4 Lithium Tetrachlorocobaltate/ Trilling X-Ray Structure Determination/Neutron Powder Diffraction/Phase Transitions. *Zeitschrift für Kristallographie* **1993**, *203*, 183−197.
(48) Elder, S. H.; Doerrer, L. H.; Disalvo, F. J.; Parise, J. B.; Guyomard, D.; Tarascón, J. M. $LiMoN_2$: The First Metallic Layered Nitride. *Chem. Mater.* **1992**, *4*, 928−937.
(49) Takada, K.; Inada, T.; Kajiyama, A.; Kouguchi, M.; Kondo, S.; Watanabe, M. Research on Highly Reliable Solid-State Lithium Batteries in NIRIM. *J. Power Sources* **2001**, *97*−*98*, 762−764.
(50) McCalla, E.; Sougrati, M. T.; Rousse, G.; Berg, E. J.; Abakumov, A.; Recham, N.; Ramesha, K.; Sathiya, M.; Dominko, R.; Van Tendeloo, G.; Novák, P.; Tarascon, J. M. Understanding the Roles of Anionic Redox and Oxygen Release during Electrochemical Cycling of Lithium-Rich Layered Li_4FeSbO_6. *J. Am. Chem. Soc.* **2015**, *137* (14), 4804−4814.
(51) Gong, Z.; Yang, Y. Recent Advances in the Research of Polyanion-Type Cathode Materials for Li-Ion Batteries. *Energy Environ. Sci.* **2011**, *4* (9), 3223.
(52) Corrao, A. A.; Mattei, G. S.; Coaty, C. M.; Li, Z.; Petrova, V.; Yin, L.; Liu, P.; Khalifah, P. G. Salt-Mediated Coarsening in Conversion-Reaction-Synthesized Nanoporous Metals and Nanocomposites Resolved through In Situ Synchrotron Diffraction Studies. *Chem. Mater.* **2023**, *35* (13), 4911−4921.
(53) Petrova, V.; Corrao, A. A.; Wang, S.; Xiao, Y.; Chapman, K. W.; Fullerton, E. E.; Khalifah, P. G.; Liu, P. Synthesis of Flexible Co Nanowires from Bulk Precursors. *RSC Adv.* **2022**, *12* (33), 21153−21159.
(54) Dobashi, S.; Hashizaki, K.; Yakuma, H.; Hirai, T.; Yamaki, J.; Ogumi, Z. Suppression of Self-Discharge by a $LiPF_6$ /Methyl Difluoroacetate Electrolyte in Li/$CuCl_2$ Batteries. *J. Electrochem. Soc.* **2015**, *162* (14), A2747−A2752.
(55) Hashizaki, K.; Dobashi, S.; Okada, S.; Hirai, T.; Yamaki, J.; Ogumi, Z. Suppression Mechanism for Dissolution of Conversion-Type $CuCl_2$ Electrode in $LiPF_6$ /Methyl Difluoroacetate Electrolyte. *J. Electrochem. Soc.* **2019**, *166* (4), A568−A573.
(56) Dobashi, S.; Nakanishi, K.; Tanida, H.; Hashizaki, K.; Uchimoto, Y.; Hirai, T.; Yamaki, J.; Ogumi, Z. Communication—XAFS Analysis of Discharge/Charge Reactions on the Li/$CuCl_2$ Battery Cathode with $LiPF_6$ /Methyl Difluoroacetate Electrolyte. *J. Electrochem. Soc.* **2016**, *163* (5), A727−A729.
(57) Poizot, P.; Laruelle, S.; Grugeon, S.; Tarascon, J.-M. Rationalization of the Low-Potential Reactivity of 3d-Metal-Based Inorganic Compounds toward Li. *J. Electrochem. Soc.* **2002**, *149* (9), A1212.
(58) Li, L.; Jacobs, R.; Gao, P.; Gan, L.; Wang, F.; Morgan, D.; Jin, S. Origins of Large Voltage Hysteresis in High-Energy-Density Metal Fluoride Lithium-Ion Battery Conversion Electrodes. *J. Am. Chem. Soc.* **2016**, *138* (8), 2838−2848.
(59) Morcrette, M.; Rozier, P.; Dupont, L.; Mugnier, E.; Sannier, L.; Galy, J.; Tarascon, J.-M. A Reversible Copper Extrusion−Insertion Electrode for Rechargeable Li Batteries. *Nat. Mater.* **2003**, *2* (11), 755−761.
(60) Kanno, R.; Takeda, Y.; Takahashi, A.; Yamamoto, O.; Suyama, R.; Koizumi, M. New Double Chloride in the LiCl-$CoCl_2$ System. *J. Solid State Chem.* **1987**, *71* (1), 189−195.
(61) Loon, C. J. J.; Ijdo, D. J. W. The Crystal Structure of Na_6MnCl_8 and $Na_2Mn_3Cl_8$ and Some Isostructural Compounds. *Acta Crystallogr. B* **1975**, *31* (3), 770−773.
(62) Goodyear, J.; Ali, S. A. D.; Steigmann, G. A. The Crystal Structure of Na_2MnCl_4. *Acta Crystallogr. B* **1971**, *27* (8), 1672−1674.

https://doi.org/10.1021/jacs.4c13005
J. Am. Chem. Soc. 2024, 146, 32059−32071